



**HAL**  
open science

## Surface morphology in tungsten and RAFM steel exposed to helium plasma in PSI-2

Ryuichi Sakamoto, Elodie Bernard, Arkadi Kreter, Céline Martin, Bernard Pegourié, Grégory Pieters, Bernard Rousseau, Christian Grisolia, Naoaki Yoshida

► **To cite this version:**

Ryuichi Sakamoto, Elodie Bernard, Arkadi Kreter, Céline Martin, Bernard Pegourié, et al.. Surface morphology in tungsten and RAFM steel exposed to helium plasma in PSI-2. *Physica Scripta*, 2017, T170, pp.014062. 10.1088/1402-4896/aa93a2 . hal-01795072

**HAL Id: hal-01795072**

**<https://hal.science/hal-01795072>**

Submitted on 18 May 2018

**HAL** is a multi-disciplinary open access archive for the deposit and dissemination of scientific research documents, whether they are published or not. The documents may come from teaching and research institutions in France or abroad, or from public or private research centers.

L'archive ouverte pluridisciplinaire **HAL**, est destinée au dépôt et à la diffusion de documents scientifiques de niveau recherche, publiés ou non, émanant des établissements d'enseignement et de recherche français ou étrangers, des laboratoires publics ou privés.

# Surface morphology in tungsten and RAFM steel exposed to helium plasma in PSI-2

Ryuichi Sakamoto<sup>1,7,§</sup>, Elodie Bernard<sup>2</sup>, Arkadi Kreter<sup>3</sup>,  
Céline Martin<sup>4</sup>, Bernard Pégourié<sup>2</sup>, Gregory Pieters<sup>5</sup>,  
Bernard Rousseau<sup>5</sup>, Christian Grisolia<sup>2,8</sup> and Naoaki Yoshida<sup>6</sup>

<sup>1</sup> NINS, National Institute for Fusion Science, Toki, Gifu 509-5292, Japan

<sup>2</sup> CEA, IRFM, F-13108 Saint-Paul-lez-Durance, France

<sup>3</sup> Forschungszentrum Jülich GmbH, Institut für Energie- und Klimaforschung -  
Plasmaphysik, 52425 Jülich, Germany

<sup>4</sup> Université Aix-Marseille, PIIM, 13397 Marseille, France

<sup>5</sup> CEA Saclay, SCBM, F-91191 Gif-sur-Yvette, France

<sup>6</sup> Kyushu University, RIAM, Kasuga, Fukuoka 816-8580, Japan

<sup>7</sup> The Graduate University for Advanced Studies, Toki, Gifu 509-5292, Japan

<sup>8</sup> National Research Nuclear University “MEPhI”, Moscow, 115409 Russian  
Federation

**Abstract.** Impact of the helium plasma exposure on the surface modification in tungsten and RAFM (Reduced Activation Ferritic/Martensitic) steel have been investigated on the linear plasma device PSI-2 assuming the condition of DEMO first wall. In tungsten, a nanoscale undulating surface structure, which has a periodic arrangement, is formed under low temperature conditions below fuzz nanostructure formation threshold  $\sim 1000$  K. Interval and direction of the undulation shows dependence on the crystal orientation. A large variation in surface level up to 200 nm has been observed among grains at a fluence of  $3 \times 10^{26}$  He/m<sup>2</sup> showing dependence of the surface erosion rate on the crystal orientation. The {100} plane in which the undulating surface structure is not formed shows the highest erosion rate. This significant erosion is due to the multistage sputtering through impurity. In RAFM steel, sponge-like nanostructure is developed and it grows with increasing helium fluence beyond 1  $\mu\text{m}$ . In the sponge-like nanostructure, a composition change from the base material is observed in which the tungsten ratio increases while the iron ratio decreases showing differences in sputtering ratio depending on the atomic mass.

Submitted to: *Phys. Scr.*

## **1. Introduction**

In a demonstration fusion plant (DEMO), tungsten is a primary candidate for plasma facing materials, which are exposed not only to hydrogen isotope fuel but also to helium ash from the burning plasma, due to its excellent high temperature properties, high sputtering threshold energy, low hydrogen retention and acceptable induced radioactivity [1]. Assuming tungsten use conditions at the first wall, which is exposed to the radiation and charge exchange particles from the main plasma and scrape-off-layer (SOL) plasma, the total incident particle flux is estimated as  $10^{21} - 10^{22}$  particles/m<sup>2</sup>/s, and several % of helium will be part of the incident flux. From the viewpoint of protection of the in vessel components from the above mentioned heat and particle load, a robust first wall will be required. At the same time, from the viewpoint of maximization of the tritium breeding ratio in the blanket, minimization of neutron attenuation will be required by reducing the thickness of the tungsten first wall. Consequently, only a thin tungsten coating layer (sub mm to few mm) on the blanket surface is envisaged as the first wall to protect the blanket from the incident heat and particles [2,3]. The lifetime of the blanket, therefore, will be affected by erosion characteristics of the tungsten first wall. Since Reduced Activation Ferritic/Martensitic (RAFM) steels are presently considered as a primary candidates for structural materials of the blanket in a demonstration fusion plant, tolerance of RAFM steel to the plasma exposure is another issue for the unexpected situation in which the tungsten first wall is removed accidentally.

Over the past decade a considerable number of studies have been made on tungsten as a plasma facing material from both experimental and theoretical aspect [4, 5]. These results show strong impact of the helium exposure on surface modifications of tungsten even at low incident energy below the displacement damage threshold. These results imply the importance of helium effects on tungsten as a plasma facing material. Considering the first wall structure, the operational temperature should be limited by the maximum allowable temperature of the blanket, that is  $\sim 823$  K in the case in which the RAFM steel is chosen as a blanket structure material [6]. This temperature is significantly below the lower threshold of the fuzz nanostructure formation, that is,  $\sim 1000$  K [7]. Although a large number of studies have been conducted on the fuzz nanostructure [7–10], little attention has been given to such low temperature ranges [11]. This motivates us to investigate helium exposure at relatively low temperature.

In this study, we have investigated helium exposure effect on tungsten and RAFM steel at the operational temperature of a demonstration fusion plant ( $\sim 800$  K) using the linear plasma device PSI-2. The samples exposed to helium plasma have been analyzed from the viewpoint of micro-structural morphology of the material surface.

## **2. Experimental setup**

For tungsten, high-purity tungsten (> 99.995 %, Toho Kinzoku Co. Ltd.) samples were mechanically polished and then annealed at 1773 K under vacuum conditions for 2 h in order to obtain a several 10  $\mu\text{m}$  monocrystal grain for the surface analysis, releasing rolling stress and enhancing recrystallization. For RAFM steel, JLF-1 (Japanese Low activation Ferritic steel) JOYO-II HEAT, which compositions are Fe, 9.00 wt% Cr, 1.98 wt% W, 0.49 wt% Mn, 0.20 wt% V, 0.083 wt% Ta, 0.09 wt% C, were mechanically polished and then finished by electrolytic polishing for removing a mechanical processing affected layer. The dimensions of both tungsten and RAFM steel samples are 7 mm  $\times$  7 mm square and 0.3 mm thick.

Helium exposure experiments were carried out using linear plasma device PSI-2 [12]. Typical incident helium energy was mono-energetic 75 eV. This incident helium energy is slightly lower than the threshold energy of the sputtering yield for tungsten [13, 14], while it is above the threshold energy for RAFM. The sample temperature was controlled to around 800 K by a combination of forced water cooling and electric heaters, taking into account the heat flux from the plasma. The sample temperature was measured by an infrared (IR) camera and cross-checked with a thermocouple installed under the sample. Two tungsten and two RAFM steel samples, four samples in total, were fixed at the sample-holder by a bolted molybdenum mask plate and exposed to helium plasma at a flux of  $\sim 1.6 \times 10^{22}$  He/m<sup>2</sup>/s.

The helium exposure effects on tungsten and RAFM steel have been investigated from the viewpoint of micro-structural morphology using the multi surface analysis techniques, including transmission and scanning electron microscopy (TEM, STEM and SEM), energy dispersive X-ray spectrometry (EDS), focused ion beam (FIB), electron backscatter diffraction (EBSD), and confocal laser microscopy (CLM).

## **3. Helium exposure impact on surface modification**

### *3.1. Tungsten*

A nanoscale undulating surface structure, which has a periodic arrangement, is formed at temperature below fuzz formation threshold  $\sim 1073$  K. The direction and the interval of the undulating surface structure depend on the crystal orientation of the grain. The previous study shows that the crests of undulation, which have  $\sim 8$  nm height, align with the  $\langle 100 \rangle$  direction [15]. Figure 1 shows the relationship between the crystal orientation and the interval of the undulating structure. The crystal orientation is expressed as a tilting angle from the  $\{100\}$  plane. The undulating surface structure is not formed near the  $\{100\}$  plane, and the wide undulating surface structure appears. As the tilting angle becomes larger toward  $\{110\}$  plane ( $45.0^\circ$ ) and  $\{111\}$  plane ( $54.7^\circ$ ), the interval of the undulation gradually becomes narrower, and is narrowest ( $\sim 25$  nm) near the  $\{110\}$  plane. The interval should also be the narrowest near the  $\{111\}$  plane considering the trend of the plot.

Figure 2 (a) shows typical SEM image of the grain boundary between grains, which have surface near the  $\{100\}$  and the  $\{110\}$  plane, at a fluence of  $3 \times 10^{26}$  He/m<sup>2</sup>. In addition to the undulating surface structure, which is developed in the right hand side grain, holes (small black dot contrast) and flakes (small white dot contrast) which originate from the aggregation of the helium bubbles are observed all over the surface, showing the possibility of nano-dust generation. Hole and flake, which are developed from the aggregation of the helium bubbles, are shown in Figure 2 (b).

The undulating surface structure begins to form at a fluence above  $10^{24}$  He/m<sup>2</sup>, and its development is almost saturated at a fluence above  $10^{25}$  He/m<sup>2</sup>. On the other hand, surface erosion should continue to progress during exposure because large variations in surface level among grains have been observed by the SEM images as shown in Figure 3. The black band at the center of the SEM image is carbon deposit for the FIB process to make a cross-sectional sample. From the cross-sectional observation at the grain boundary (Figure 3 (b)), the maximum difference in surface level reaches to 140 nm. This fact shows that the surface erosion rate varies depending on the crystal orientation of the grain.

Figure 4 shows histograms of the relative surface level measured by the CLM in a region of  $129 \mu\text{m}$  square with  $0.129 \mu\text{m}$  spatial resolution. In the case of  $1 \times 10^{25}$  He/m<sup>2</sup>, the width of the histogram is within 50 nm. This width is the same width as the pristine sample before the plasma exposure. Therefore, the erosion is not obvious at fluence of  $1 \times 10^{25}$  He/m<sup>2</sup>, and it can be said that the ambiguity of the measurement, which includes the initial distortion of the sample and measurement error, is approximately 50 nm. The histogram width becomes wider with increasing helium fluence, 120 nm at  $1 \times 10^{26}$  He/m<sup>2</sup> and 200 nm at  $3 \times 10^{26}$  He/m<sup>2</sup>, showing an increase of erosion. There are three obvious peaks in the histogram as shown by vertical arrows and plotted in Figure 4. This peak may indicate three groups of specific crystal orientations. Since the peak height can be affected by not only the crystal orientation dependence of the erosion but also the initial distribution of the crystal orientation, additional information on the crystal orientation is required for a full understanding.

In order to investigate a crystal orientation dependence of the erosion rate, crystal orientation mapping by the EBSD analysis and surface level mapping by the CLM analysis have been compared. Figure 5 (a) shows SEM image, crystal orientation map and surface level map of the identical area. The distribution of crystal orientation and relative grain size within the area of interest are indicated in the orientation triangle (Figure 5 (b)). Moreover, the distribution of crystal orientation is projected against the surface tilting angle from the  $\{100\}$  plane in Figure 5 (c). The  $\{100\}$  and  $\{111\}$  planes correspond to the  $45.0^\circ$  and  $54.7^\circ$  in the surface tilting angle. As is obvious from the crystal orientation map which is dominated by red color, the crystal orientation is broadly concentrated near the  $\{100\}$  plane (distribution peak at  $10^\circ - 15^\circ$ ) and mainly spreads to the  $\{111\}$  plane. This may be the texture due to the recrystallization process at the sample preparation. Nevertheless, there is a green color grain which shows the  $\{110\}$  plane. Therefore, whole orientation grains are contained within the area

of interest. The area of the circles in Figure 5 (b) relatively corresponds with the grain size (area), which is distributed between 5 - 1500  $\mu\text{m}^2$ . There is no clear dependence of the grain size on crystal orientation.

The relative surface level, which is measured by the CLM, is plotted against the surface tilting angle from the  $\{100\}$  plane in Figure 6. At the  $\{100\}$  plane, where the nanoscale undulating surface structure cannot be formed, the surface level is the minimum level which shows that the surface erosion reached the maximum. And the relative surface level is increased proportionally as the tilting angle increases. At the  $\{110\}$  and the  $\{111\}$  planes where the nanoscale undulating surface structure is formed, the surface level is relatively high, showing that the erosion rate is slower than the  $\{100\}$  plane. It became clear that the large difference in surface level up to 200 nm is formed at a fluence of  $3 \times 10^{26}$  He/m<sup>2</sup> due to the crystal orientation impact on the surface erosion rate. The highest erosion yield for the grains with orientation close to the  $\{100\}$  is also observed in the Ar or Ne seeding deuterium plasma exposure experiments [16]. On the other hand, theoretical study [14] predicted that the  $\{110\}$  plane have a significantly higher sputtering yield than the  $\{100\}$  plane or the  $\{111\}$  plane, because the  $\{110\}$  plane is the most closely-packed of the three, and hence most likely to produce a direct helium–tungsten collision.

Despite the fact that there is a large erosion up to 200 nm at a fluence of  $3 \times 10^{26}$  He/m<sup>2</sup>, the undulating surface structure, which has small scale structures which are less than 10 nm, remains unchanged. Therefore, the undulating surface structure achieves stable equilibrium.

### *3.2. RAFM steel*

Figure 7 shows typical surface damage structure of RAFM steel (JLF-1) with He plasma exposure at a fluence of  $1 \times 10^{25}$  He/m<sup>2</sup> and  $3 \times 10^{26}$  He/m<sup>2</sup>, from the top to the bottom, (a), (d) lower-magnification SEM images, (b), (e) higher-magnification SEM images, and (c), (f) cross-sectional STEM image at the same magnification with higher-magnification SEM image. In order to protect a complex damage structure from the FIB processing, at first carbon deposit layer was made on the sample surface, then tungsten deposit layer was made on the carbon layer before the cross-sectional processing with FIB. Since the carbon deposition could not enter deep inside the complex damage structure, only the top of the damage structure is covered by the carbon deposition, and still there are empty spaces at the bottom of the damage structure. At the fluence of  $1 \times 10^{25}$  He/m<sup>2</sup>, the lower-magnification SEM image remains unchanged from the unexposed samples. However, sponge-like complex damage structure which have 500 nm depth are developed (Figure 7 (b), (c)). When the fluence increases to  $3 \times 10^{26}$  He/m<sup>2</sup>, a larger-scale round shape structure with 1 – 2  $\mu\text{m}$  size is developed (Figure 7 (d)), and the sponge-like structure grows in the depth direction beyond 1  $\mu\text{m}$  (Figure 7 (f)). Similar surface modification was observed in the the deuterium plasma exposed RAFM steel, F82H and EUROFER-97 [17, 18]. In the case of the deuterium exposure, however, the

depth of the damaged layer is less than half of the one of the helium exposure case. Furthermore, no bubbles are observed in the case of deuterium plasma exposure. In contrast, the sponge-like structure filled up with many bubbles as is clear from Figure 7 (f). It should be noted that there is a clear boundary between the sponge-like structure and bulk material, and almost no bubbles can be observed in the bulk side.

Figure 8 shows composition mapping with STEM-EDS analysis. The intensity of each map is of relative value with respect to each element. In the left upper corne of tungsten EDS map (red), the signal intensity is high even though it should be dark as well as the other maps. This tungsten signal is due to the surface protection layer, which consists of the double layers of carbon and tungsten, on the sample surface for the FIB processing. In the bulk material, according to the EDS quantitative analysis, the composition ratio of iron, chromium and tungsten are 88 %, 10 % and 2 % as a natural result from the composition of JLF-1. In the sponge-like structure, there is considerable reduction of the iron intensity from the bulk material. The chromium intensity was also reduced. The tungsten intensity, however, remains unchanged between bulk and sponge-like structure. Consequently, tungsten ratio increases up to 33 % in the sponge-like structure showing differences in sputtering ratio depending on the atomic mass. Similar tungsten surface enrichment is also reported on the deuterium plasma exposed RAFM steel F82H [17] and EUROFER [19].

Special attention should be paid to the detection of molybdenum, which is an extrinsic element of JLF-1, on the sponge-like structure showing impurity deposition. Since the possibility of contamination with molybdenum during the FIB processing has been eliminated in this study, a feasible explanation for the molybdenum deposition is that the sputtered molybdenum come from other than the samples during helium plasma exposure. The molybdenum source should be the mask plate and/or the bolt of the sample holder. The existence of molybdenum impurity during exposure makes understanding of surface modifications difficult because such a heavy impurity may have strong impact on the surface modification by increasing sputtering yield. This matter is taken up in the next section.

#### **4. Discussion**

Previous theoretical and experimental studies show that the threshold energy of helium to sputter tungsten is above 105 eV [13, 14]. Therefore, no erosion is expected in our experimental conditions. Unexpectedly large erosion rate, however, is observed in the low energy helium plasma exposure below the threshold energy of sputtering. Therefore, the erosion rate is too large to explain with only impact of helium exposure.

The surface level variation could be explained by the swelling of some grain due to the helium bubble formation. However, because the range of helium bubble formation is up to several 10 nm depth which is considerably shallower than erosion depth, it could not be the main effect. Furthermore, helium bubble distributes equally all over the plasma exposed surface.

One feasible explanation for the unexpected erosion may be that there is a sputtering enhancement effect with heavier elements, which originate from RAFM steel sample. Since tungsten samples were exposed to helium plasma together with RAFM steel samples, iron and chromium, which can be sputtered by low energy helium plasma, may get mixed in the plasma as an impurity. If so, then such a heavy impurity has the potential to sputter molybdenum and tungsten. If a simple two-body collision is assumed to obtain fundamental idea, the maximum energy transfer ratio from incident particle to target atom is expressed by the following equation,

$$\eta = \frac{4M_i M_t}{(M_i + M_t)^2},$$

where  $M_i$  and  $M_t$  denote mass of incident particle and target atom, respectively. The maximum energy transfer ratio of atoms of interest and maximum transferring energy from incident particle with an energy of 75 eV are summarized in Table 1. Since the surface binding energy of tungsten is 8.8 – 11.75 eV [20,21], the maximum transferring energy of 75 eV helium to tungsten (6.3 eV) is insufficient for yielding sputtering, while the maximum transferring energy to iron (18.7 eV) is sufficient for yielding sputtering. Furthermore, a part of molybdenum mask plate is also exposed to plasma, and the maximum transferring energy of 75 eV helium to molybdenum (11.5 eV) is marginal for yielding sputtering. Once impurities mixed into the plasma, the energized impurities will strike the target with the efficient energy transfer ratio. For example, the maximum transferring energy of 75 eV iron to tungsten and molybdenum are 53.6 eV and 69.8 eV. The above-mentioned multistage sputtering is supported by the fact that the unexpected tungsten erosion is observed when tungsten was exposed by helium plasma together with the RAFM steel samples. Clear erosion cannot be observed in the case of the tungsten-only exposure to helium plasma, or in the case of deuterium majority plasma exposure even together with the RAFM steel samples.

Erosion enhancement with the multistage sputtering seems likely to occur in DEMO, because it will be mandatory to inject impurity gas for the divertor detachment [22]. In addition to exposure to the low temperature SOL plasma, higher energy charge exchange particles from the high-density and high-temperature main plasma will enhance the impurity generation. Careful consideration is required for the design of the surface materials of the plasma facing components including all in-vessel components which are situated at a remote area.

## 5. Conclusion

In tungsten, crystal orientation has a impact on surface structural modification and erosion. The nanoscale undulating surface structure, which align with  $\langle 100 \rangle$  directions, is formed depending on crystal orientation at temperatures below fuzz formation threshold. Near the  $\{100\}$  plane, the undulating surface structure cannot develop and significant erosion around 200 nm at  $3 \times 10^{26}$  He/m<sup>2</sup> is observed. As a grain surface tilt



from {100} plane, the interval of undulating surface structure becomes narrower and erosion gradually becomes suppressed.

In general, significant tungsten erosion was not expected with a low energy helium exposure. In this study, however, significant erosion with helium plasma exposure accidentally occurs owing to the material combination used in the experiment, that is, the presence of RAFM steel. This result warns of an erosion enhancement due to the multistage sputtering effects on the plasma facing materials in a real device which will consist of several materials.

In RAFM steel (JLF-1), the helium exposed surface is damaged considerably deep and a sponge-like structure, which is filled with helium bubbles, is developed. The sponge-like structure becomes deeper with increasing fluence and it reaches a depth of  $1\ \mu\text{m}$  at  $3 \times 10^{26}\ \text{He}/\text{m}^2$ . A composition change from the base material is observed in which the tungsten ratio increases while the iron ratio decreases showing a selective sputtering depending on the atomic mass. It seems that the RAFM steel has low tolerance for plasma exposure and an adequate armor is required to use as a plasma facing material in the demonstration fusion plant not only for preventing damages but also for suppressing impurity generation.

## Acknowledgments

The authors are grateful to the staff of the PSI-2 team for their experimental support and to Mr. D. Nagata for preparing the TEM samples. The JLF-1 JOYO-II HEAT samples are provided by Dr. T. Nagasaka. This work is supported by the IEA Technology Collaboration Programme on the Development and Research on Plasma Wall Interaction Facilities for Fusion Reactors (PWI TCP).

## References

- [1] G. Pintsuk, "Tungsten as a plasma-facing material", Reference Module in Comprehensive Nuclear Materials, Vol. 4, pp. 551-581 (2012). <http://doi.org/10.1016/B978-0-08-056033-5.00118-X>
- [2] Y. Someya, K. Tobita, H. Utoh, S. Tokunaga, K. Hoshino, N. Asakura, M. Nakamura, Y. Sakamoto, "Design study of blanket structure based on a water-cooled solid breeder for DEMO", Fusion Engineering and Design 98-99 (2015) 1872-1875. <http://doi.org/10.1016/j.fusengdes.2015.05.042>
- [3] P. Pereslavytsev, C. Bachmann and U. Fischer, "Neutronic analyses of design issues affecting the tritium breeding performance in different DEMO blanket concepts", Fusion Engineering and Design (2015), In Press. <http://doi.org/10.1016/j.fusengdes.2015.12.053>
- [4] J. Roth, E. Tsitron, A. Loarte, T. Loarer, G. Counsell, R. Neu, V. Philipps, S. Brezinsek, M. Lehnen, P. Coad, Ch. Grisolia, K. Schmid, K. Krieger, A. Kallenbach, B. Lipschultz, R. Doerner, R. Causey, V. Alimov, W. Shu, O. Ogorodnikova, A. Kirschner, G. Federici, A. Kukushkin, "Recent analysis of key plasma wall interactions issues for ITER", Journal of Nuclear Materials 390-391 (2009) 1-9. <http://doi.org/10.1016/j.jnucmat.2009.01.037>
- [5] B.D. Wirth, K.D. Hammond, S.I. Krasheninnikov, D. Maroudas, "Challenges and opportunities of modeling plasma-surface interactions in tungsten using high-performance computing", Journal of Nuclear Materials 463 (2015) 30-38. <http://doi.org/10.1016/j.jnucmat.2014.11.072>

- [6] E. Lucon, P. Benoit, P. Jacquet, E. Diegele, R. Lässer, A. Alamo, R. Coppola, F. Gillemot, P. Jung, A. Lind, S. Messoloras, P. Novosad, R. Lindau, D. Preininger, M. Klimiankou, C. Petersen, M. Rieth, E. Materna-Morris, H.-C. Schneider, J.-W. Rensman, B. van der Schaaf, B.K. Singh, P. Spaetig "The European effort towards the development of a demo structural material: Irradiation behaviour of the European reference RAFM steel EUROFER", *Fusion Engineering and Design* 81 (2006) 917-923. <http://doi.org/10.1016/j.fusengdes.2005.08.044>
- [7] S. Kajita, W. Sakaguchi, N. Ohno, N. Yoshida and T. Saeki, "Formation process of tungsten nanostructure by the exposure to helium plasma under fusion relevant plasma conditions", *Nuclear Fusion* 49 (2009) 095005. <http://doi.org/10.1088/0029-5515/49/9/095005>
- [8] G. De Temmerman, K. Bystrov, J.J. Zielinski, M. Balden, G. Matern, C. Arnas and L. Marot, "Nanostructuring of molybdenum and tungsten surfaces by low-energy helium ions", *Journal of Vacuum Science & Technology A* 30 (2012) 041306. <http://doi.org/10.1116/1.4731196>
- [9] M.J. Baldwin, R.P. Doerner, "Helium induced nanoscopic morphology on tungsten under fusion relevant plasma conditions", *Nuclear Fusion* 48 (2008) 035001. <http://doi.org/10.1088/0029-5515/48/3/035001>
- [10] S. Takamura and Y. Uesugi, "Experimental identification for physical mechanism of fiber-form nanostructure growth on metal surfaces with helium plasma irradiation", *Applied Surface Science* 356 (2015) 888-897. <http://doi.org/10.1016/j.apsusc.2015.08.112>
- [11] M. Miyamoto, S. Mikami, H. Nagashima, N. Iijima, D. Nishijima, R.P. Doerner, N. Yoshida, H. Watanabe, Y. Ueda, A. Sagara, "Systematic investigation of the formation behavior of helium bubbles in tungsten", *Journal of Nuclear Materials* 463 (2015) 333-336. <http://doi.org/10.1016/j.jnucmat.2014.10.098>
- [12] A. Kreter, C. Brandt, A. Huber, S. Kraus, S. Möeller, M. Reinhart, B. Schweer, G. Sergienko and B. Unterberg, "Linear Plasma Device PSI-2 for Plasma-Material Interaction Studies", *Fusion Science and Technology* 68 (2015) 8-14. <http://doi.org/10.13182/FST14-906>
- [13] R.E.H. Clark, (Ed.), "Atomic and Plasma-Material Interaction Data for Fusion", vol. 7B, International Atomic Energy Agency, Vienna, 2001, STI/PUB/023/APIID/07/B.
- [14] F. Ferroni, K.D. Hammond, B.D. Wirth, "Sputtering yields of pure and helium-implanted tungsten under fusion-relevant conditions calculated using molecular dynamics", *Journal of Nuclear Materials* 458 (2015) 419-424. <http://doi.org/10.1016/j.jnucmat.2014.12.090>
- [15] R. Sakamoto, E. Bernard, A. Kreter, N. Yoshida, "Surface morphology of tungsten exposed to helium plasma at temperatures below fuzz formation threshold 1073 K", *Nuclear Fusion* 57 (2016) 016040. <http://doi.org/10.1088/1741-4326/57/1/016040>
- [16] M. Rasinski, A. Kreter, Y. Torikai, C. Linsmeier, "The microstructure of tungsten exposed to D plasma with different impurities", *Nuclear Materials and Energy*. *in press* <http://doi.org/10.1016/j.nme.2016.11.001>
- [17] V.K. Alimov, Y. Hatano, N. Yoshida, H. Watanabe, M. Oyaidzu, M. Tokitani and T. Hayashi, "Surface modification and sputtering erosion of reduced activation ferritic martensitic steel F82H exposed to low-energy, high flux deuterium plasma", *Nuclear Materials and Energy* 7 (2016) 25-32. <http://doi.org/10.1016/j.nme.2016.01.001>
- [18] M. Rasinski, S. Möller, J. Steffens, B. Unterberg, K. Sugiyama, T. Schwarz-Selinger, A. Kreter, C. Linsmeier, "Morphology and composition of Fe-W coatings after deuterium plasma exposure as a model system for RAFM steels", *Physica Scripta T167* (2016) 014013. <http://doi.org/10.1088/0031-8949/2016/T167/014013>
- [19] J. Roth, K. Sugiyama, V. Alimov, T. Höschen, M. Baldwin and R. Doerner, "EUROFER as wall material: Reduced sputtering yields due to W surface enrichment", *Journal of Nuclear Materials* 454 (2014) 1-6. <http://doi.org/10.1016/j.jnucmat.2014.07.042>
- [20] G.M. McCracken, "The behaviour of surfaces under ion bombardment", *Reports on Progress in Physics* 38 (2001) 241-327. <http://doi.org/10.1088/0034-4885/38/2/002>
- [21] X. Yang, A. Hassanein, "Atomic scale calculations of tungsten surface binding energy and beryllium-induced tungsten sputtering", *Applied Surface Science* 293 A (2014) 187-190.

<http://doi.org/10.1016/j.apsusc.2013.12.129>

- [22] N. Asakura, K. Shimizu, K. Hoshino, K. Tobita, S. Tokunaga, T. Takizuka, "A simulation study of large power handling in the divertor for a Demo reactor", *Nuclear Fusion* 53 (2013) 123013. <http://doi.org/10.1088/0029-5515/53/12/123013>

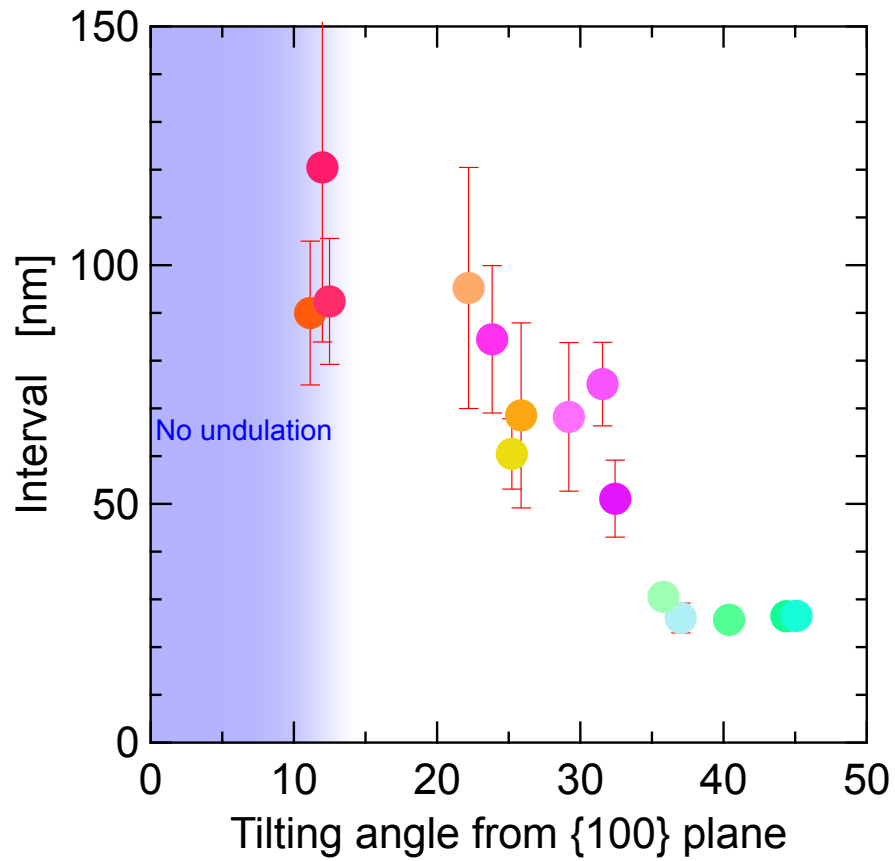


**Figure 1.** Variation of the averaged interval of undulations with the grain surface orientation based on the tilting angle from the {100} surface. The symbol color shows crystal orientation which is shown in the orientation triangle (Figure 5).

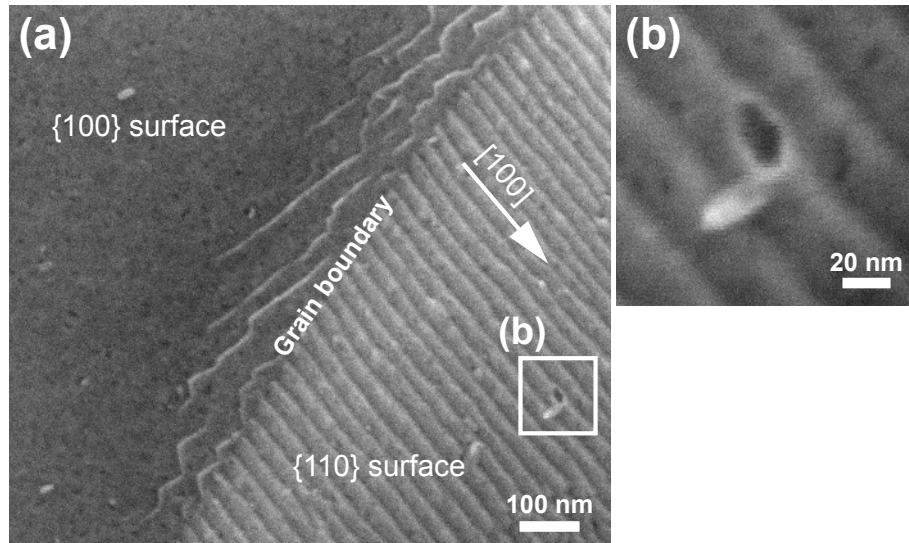


**Figure 2.** (a) SEM image of the grain boundary between grains, which have surface near the {100} and the {110} plane, at a fluence of  $3 \times 10^{26}$  He/m<sup>2</sup>. The flaking bubble is magnified in (b)

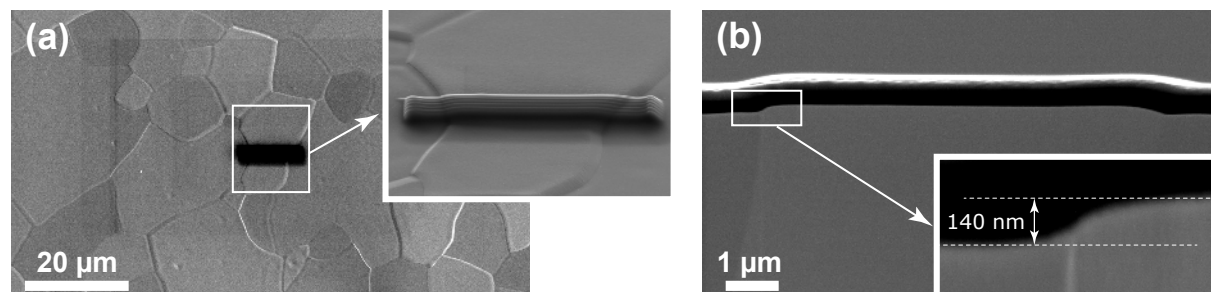


**Figure 3.** (a) SEM image of the helium plasma exposed tungsten surface at a fluence of  $3 \times 10^{26}$  He/m<sup>2</sup>. (b) Cross-sectional SEM observation at the grain boundaries. Black band on the surface is carbon deposition for protecting surface from the FIB processing.

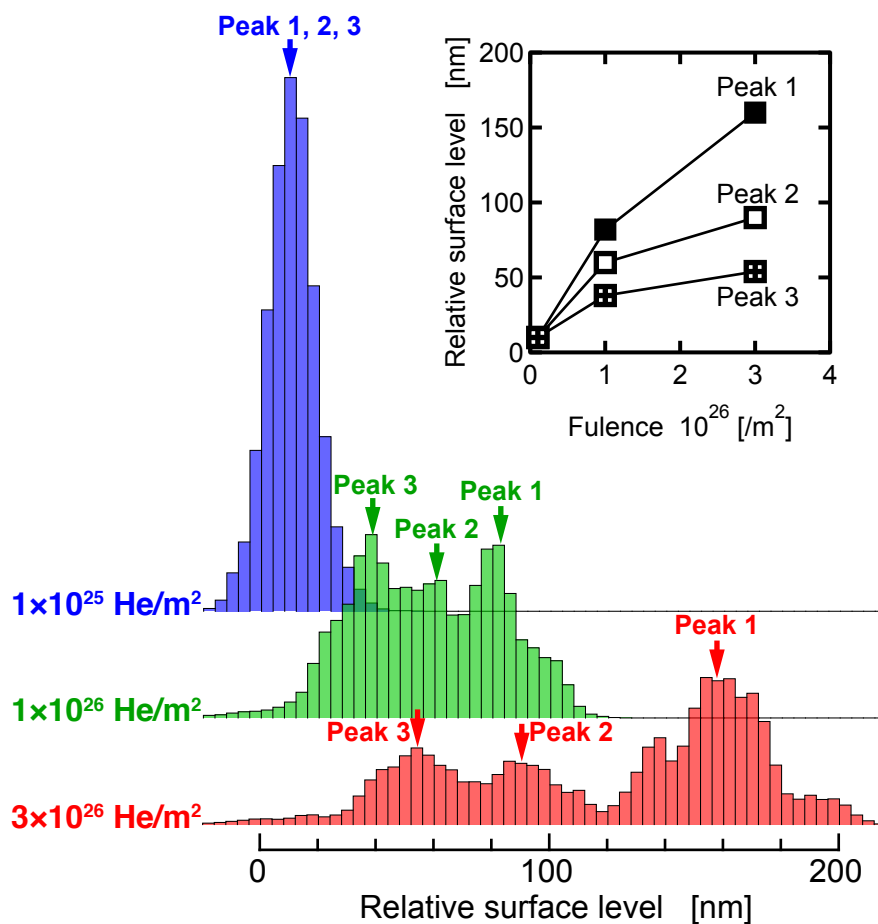


**Figure 4.** The histograms of the relative surface level at fluences of  $1 \times 10^{25} \text{ He/m}^2$ ,  $1 \times 10^{26} \text{ He/m}^2$  and  $3 \times 10^{26} \text{ He/m}^2$ . The relative surface level of the peaks are also plotted against the fluence.

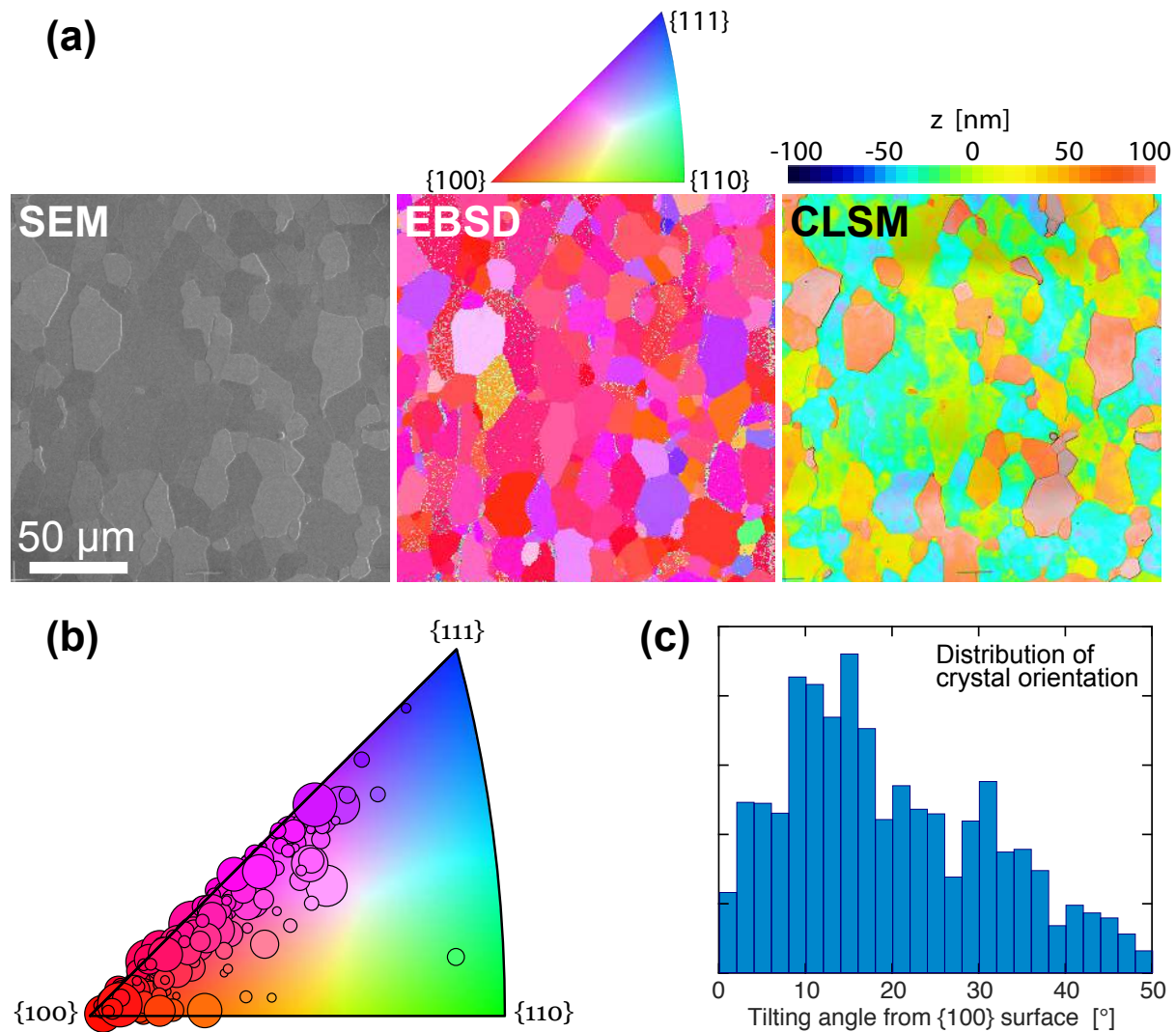


**Figure 5.** (a) Comparison among SEM image, crystal orientation and relative surface level at the same area. (b) Crystal orientation distribution in the interested area. The area of the circles relatively correspond with the area of the grains. (c) Projection of the crystal orientation distribution onto the surface tilting angle from the {100} plane.



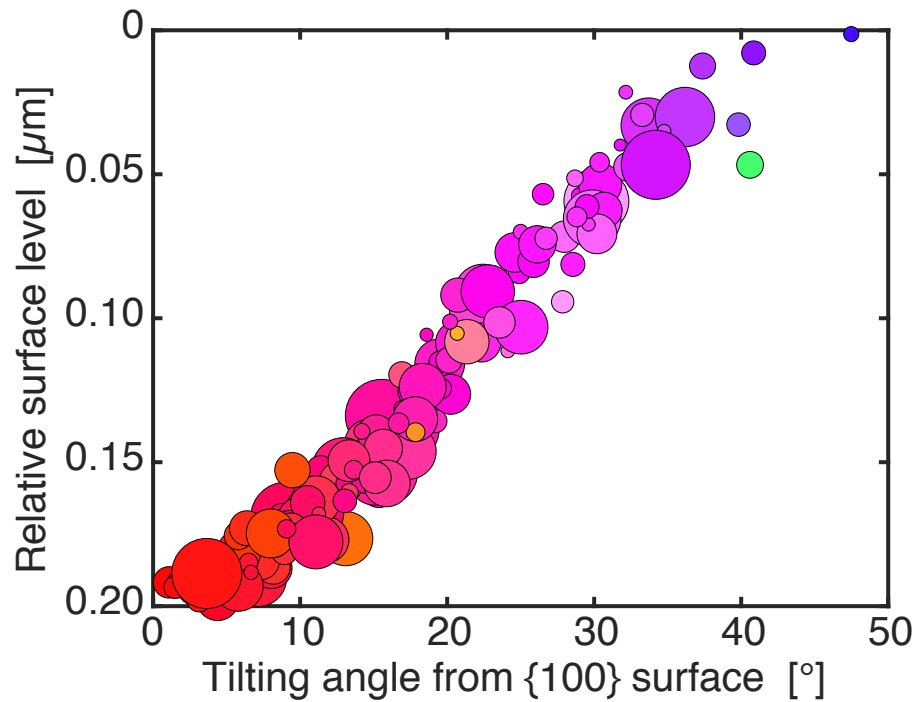


**Figure 6.** Variation of the relative surface level with the grain surface orientation based on the tilting angle from the {100} surface. The area of the circles relatively correspond with the area of the grains.

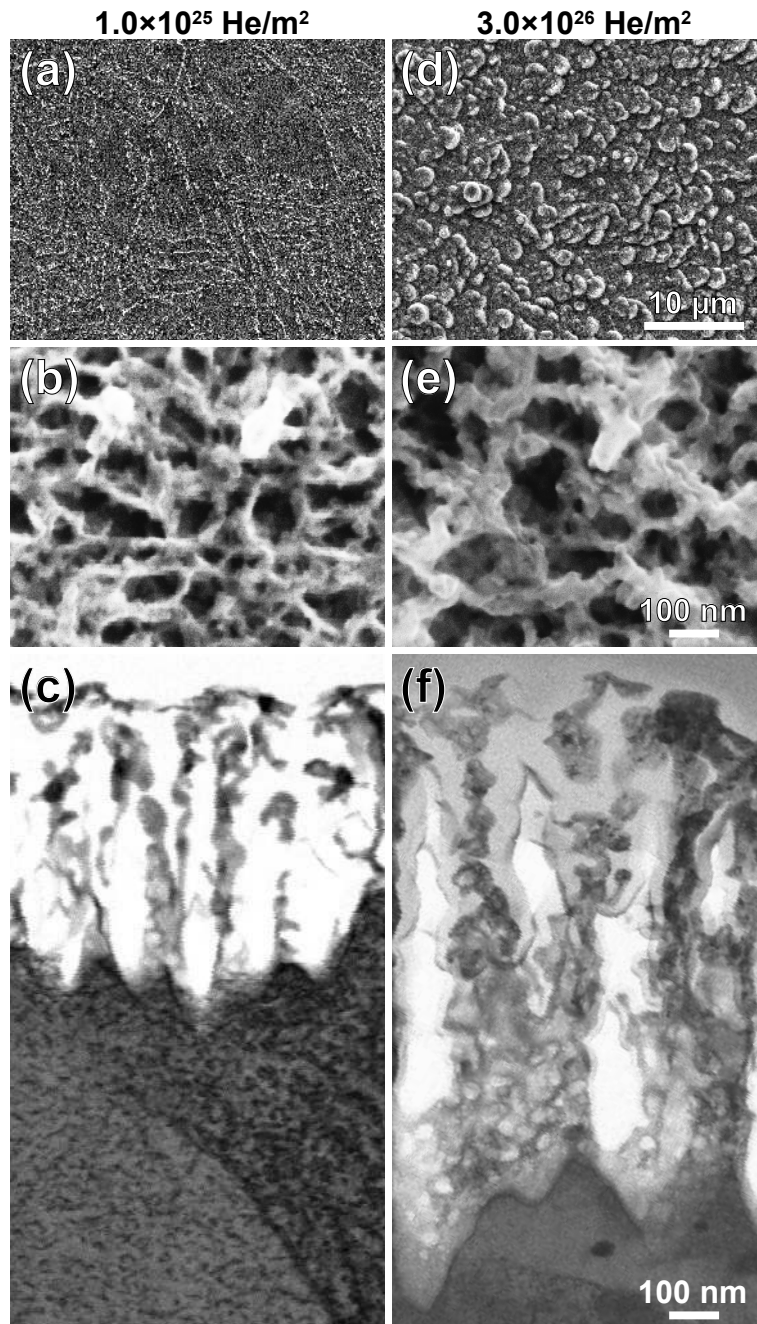


**Figure 7.** Typical surface damage structure of RAFM steel (JLF-1) with He plasma exposure at a fluence of  $1 \times 10^{25} \text{ He/m}^2$  and  $3 \times 10^{26} \text{ He/m}^2$ . (a), (d) lower-magnification surface SEM images, (b), (e) higher-magnification surface SEM images, and (c), (f) cross-sectional STEM images.

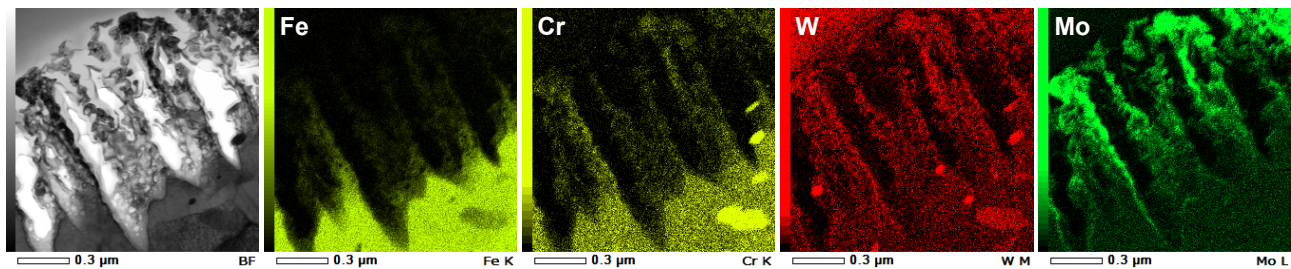


**Figure 8.** Cross-sectional STEM bright field images and EDS-maps of Fe, Cr, W and Mo for sponge-like structures of RAFM (JLF-1) surface under helium plasma exposure at a fluence of  $3 \times 10^{26}$  He/m<sup>2</sup>.

| <b>Plasma→Wall</b> | <b>Max. Energy Transfer Ratio</b> | <b>Transferring Energy @ 75 eV</b> |
|--------------------|-----------------------------------|------------------------------------|
| <b>D → W</b>       | 0.043                             | 3.2                                |
| <b>D → Mo</b>      | 0.080                             | 6.0                                |
| <b>He → W</b>      | 0.083                             | 6.3                                |
| <b>D → Fe</b>      | 0.134                             | 10.0                               |
| <b>He → Mo</b>     | 0.154                             | 11.5                               |
| <b>He → Fe</b>     | 0.249                             | 18.7                               |
| <b>Fe → W</b>      | 0.715                             | 53.6                               |
| <b>Fe → Mo</b>     | 0.930                             | 69.8                               |

**Table 1.** The maximum energy transfer ratio and maximum transferring energy from incident particle with an energy of 75 eV.